Table of Contents Entry

Hematite nanorod arrays were activated through proper control of annealing conditions. The 100-fold improvement in photocurrent was correlated with increased absorption and Sn doping from the tin oxide coated glass substrate. The low onset potential is attributed to a reduction in surface defects, while the morphology is credited for promoting tin diffusion and facilitating electron transport.

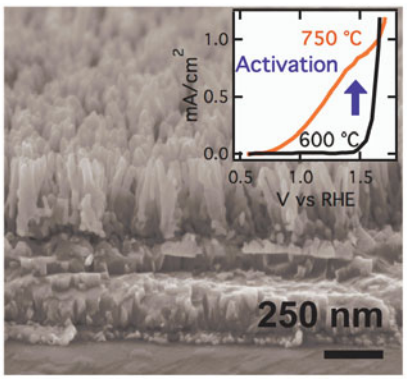

Keywords: hematite, nanorods, photochemistry, thin films

Activation of Hematite Nanorod Arrays for Photoelectrochemical Water Splitting

Rachel Morrish,[1] Mahfujur Rahman,[2] J.M. Don MacElroy,[2] Colin A. Wolden,[1,*]
[1]Department of Chemical Engineering, Colorado School of Mines, Golden, CO 80401, USA
[2]School of Chemical and Bioprocess Engineering, University College Dublin, Belfield, Dublin 4, Ireland

Hematite (α-Fe_2O_3) is a promising material for sustainable generation of H_2 due to its low cost, widespread availability, chemical stability, and its ability to absorb a significant fraction of visible light. However, numerous challenges must be overcome for this material to fulfill its theoretical potential of 15% solar to hydrogen efficiency.[1] Current performance is limited by high onset potentials coupled to low plateau current densities.[2] The first obstacle has been partially addressed by integrating electro-catalysts to accelerate the oxidation evolution reaction (OER).[2-4] Low photocurrent densities arise from a mismatch between the photon penetration depth (~100 nm)[5] and the diffusion length of photogenerated holes (2-4 nm).[6, 7] Nanostructured morphologies offer a route to improve current density by using structures with features that approach the hole diffusion length scale. For example, state-of-the-art hematite photoanodes formed by atmospheric pressure chemical vapor deposition (APCVD) have a dendritic, cauliflower-like morphology with primary particles as small as 5 nm.[8] Another successful approach employed nanotubes with a wall thickness of 7 nm produced through anodization of iron foil.[9]

A recent perspective highlighted solar fuels as one area where nanowires are expected to have a substantial impact.[10] Indeed, vertically aligned hematite nanowire arrays have been advocated as an ideal morphology for water splitting.[11] A sufficiently small diameter would alleviate hole transport limitations, while their large specific surface area would help address the intrinsically slow OER kinetics. Hematite nanorods and wires have been synthesized using chemical bath deposition (CBD)[12] and through the oxidation of iron foils.[13, 14] Unfortunately, the photoelectrochemical (PEC)

* To whom correspondence should be addressed, cwolden@mines.edu

performance of these purposefully nanostructured materials has been quite poor, with photocurrent densities no higher than 5 μA/cm^2 under standard illumination conditions.[15, 16] In this communication we show that this low performance, which is primarily attributed to poor electron transport both within the hematite and at the conducting interface, can be overcome and demonstrate the promise of nanorod architectures for photo-electrolysis of water.

A common feature of leading hematite electrodes produced through solution growth has been the requirement of a high temperature (>700 °C) annealing step for activation.[17-20] In this communication, the aqueous CBD technique for nanorod synthesis originally developed by Vayssieres et al.[12] is revisited, with a focus on the effects of the post-deposition annealing process. The biggest challenge with respect to solar fuels is developing cost effective technologies to manage terawatt levels of power.[21] CBD is compatible with this goal, offering a scalable approach for production of robust photoanodes on fluorine-doped tin oxide (FTO) coated glass using inexpensive salts without the need for organic compounds or solvents. Here we report that proper annealing conditions result in drastic performance improvements, and the underlying mechanisms for activation are interpreted by coupling detailed characterization to a systematic investigation of the process space.

Iron oxide nanorod arrays were grown on FTO-coated glass substrates by CBD using aqueous mixtures of $FeCl_3$ and $NaNO_3$ following procedures described in the literature.[12] Well-adhered films comprised of perpendicularly aligned nanorods ~200 nm in thickness were obtained using a bath temperature of 90 °C. Post deposition heating at temperatures >400 °C in air fully oxidized the nanorod films to the α-Fe_2O_3 phase as confirmed by XRD (see Fig. S1, Supplementary Information). All films display similar patterns with a prominent (110) diffraction peak, which has been suggested as the preferential orientation for electron transport in hematite.[8] Caution should be taken when heating

standard soda-lime glass to elevated temperatures (softening point ~ 715 °C); however, thermal distortion of the glass substrate was minimal using the short time scales employed.

The PEC performance of hematite electrodes after various annealing treatments is shown in Figure 1. The photocurrent was measured as a function of applied potential in 1.0 M NaOH at a scan rate of 50 mV/s under AM 1.5 illumination with an intensity of 87 mW/cm^2. Note that previous work with hematite nanorods that yielded very low photocurrents employed an hour long anneal at 550 °C.[15] Consistent with those results, the sample annealed at 600 °C for 5 minutes displayed a negligible response, indistinguishable from the dark current on this scale (not shown). However, significant photocurrents were measured in samples annealed at 700 °C, and the response was further enhanced when the temperature was raised to 750 °C. Alternatively, activation could be achieved by calcining samples for extended times at a lower temperature of 600 °C, displaying marked improvement at levels intermediate to the 5 minute treatments at 700 and 750 °C (Fig. 1).

The two most critical metrics for photoanode performance are the oxygen evolution current density (J_{OER}) and the onset potential (V_{on}), where appreciable photocurrent is first detected.[2, 21] The J_{OER} was measured at the thermodynamic water splitting potential (V = 1.23 v. RHE),[1, 2, 21] while V_{on} was determined based on the derivative of the J-V curve using the methodology adopted by the Grätzel group.[22] Activated photoanodes displayed onset potentials less than +0.75 V versus RHE. These are among the lowest onset potentials achieved for hematite photoanodes without an OER catalyst,[9, 23] about 250 mV lower than many reports.[2, 17, 20, 24] The low potential may indicate the annealed anodes contain minimal surface trapping states.[22, 23] The J_{OER} recorded as a function of annealing time and temperature is reported in the inset of Fig. 1. The 5 minute/750 °C sample has a J_{OER} = 0.52 mA/cm^2, an improvement of more than two orders of magnitude over previous work,[15, 16] and comparable to the

value achieved at this potential by the champion hematite electrode produced through solution techniques.[20] The fundamental reasons responsible for hematite activation are elaborated below.

The PEC performance was well correlated with changes in morphology, with Figure 2 displaying micrographs of the samples shown in Fig. 1. Images (a) – (c) display changes observed with temperature at a fixed annealing time of 5 minutes. Samples heated to 600 °C for 5 minutes looked nearly identical to films synthesized by CBD (Fig. S2). However, at 700 °C a dramatic change in structure was observed. There appears to be grain ripening that results in coalesced features with very smooth surfaces. Defective surfaces have been correlated with high onset potentials,[20] and the low values obtained in this work reflect the high quality of the iron oxide surface. Heating to 750 °C produced a similar morphology, though the average feature size was increased. Films exposed to extended annealing at 600 °C produced morphologies resembling those annealed for short time at elevated temperatures (Fig. 2d). The surface features in these images are similar to leading reports of hematite produced by solution grown material after high temperature annealing.[19, 25]

Despite the improvements, the J_{OER} values remain considerably short of the current standard of 2.4 mA/cm^2 achieved by APCVD without a catalyst.[2] As shown in Fig. 2, a consequence of the annealing process is that nanorods coalesce into features whose characteristic size is much greater than the hole diffusion length. Competition between activation and feature evolution is reflected by the changes in J_{OER} with time and temperature shown in the inset of Fig. 1. At 750 °C, the highest current was obtained after 5 minutes, and performance declines sharply with time as the nanostructure is lost. At 600 °C photocurrent improves steadily with time up to about 8 hours, before falling for similar reasons. The difference between peak J_{OER} obtained at 600 and 750 °C is attributed to the larger feature size obtained at the lower temperature (Fig. 2c, d). This suggests that the energy barrier associated with hematite activation is greater than that for morphology evolution, and techniques such as rapid thermal processing

may further enhance performance. Additional strategies to improve morphology include modification of the CBD process to produce nanorods with finer features at greater spacing, and the use of a silica encapsulation technique that was recently shown to preserve nanostructured hematite morphologies upon heating.[20]

Tin was detected on the hematite surface after even the mildest annealing treatment, and its intensity increased with both time and temperature. Figure 3 displays high resolution X-ray photoelectron spectra (XPS) of the Sn 3d and Fe 2p regions obtained from annealed nanorods. Tin was always present in the 4^+ state ($3d_{5/2}$ = 486.9 eV), and its increase was accompanied by a slight attenuation of the Fe signal. No tin or impurities were detected in films analyzed after the CBD process, confirming that Sn migrated from the underlying FTO layer. Surface concentrations of 3, 8, and 13% Sn on a metals basis (Sn/Sn+Fe) were obtained after 5 minute oxidations at temperatures of 600, 700, and 750 °C, respectively, reflecting the activated nature of the diffusion process. At 600 °C the tin density increased monotonically with annealing time, reaching 11% after 8 hours. Further heating of the nanorod samples beyond 600 °C/8 hr or 750 °C/5 min introduced only marginally higher Sn levels, indicating the solubility limit had been reached. Although bulk SnO_2-Fe_2O_3 systems exhibit solid solution miscibility of a mere 1% Sn, much higher solubility (11%) comparable to the values reported here have been observed in nanoparticle systems.[26, 27] FTO-coated glass is perhaps the most common substrate employed for preparation of hematite electrodes. Whether intentional or not, these results indicate that some level of Sn diffusion occurs when process temperatures ≥600 °C are employed, presumably impacting overall performance.

A more detailed examination of the XPS spectra provides insight into the nature of tin incorporation into the hematite lattice. The Fe 2p spectra revealed that iron exists predominately as Fe^{3+}, with a $2p_{3/2}$ peak position of 710.9 eV.[28] Of interest is the location of the $2p_{3/2}$ shake-up satellite peak. For moderate

heat treatments, a characteristic hematite satellite peak at approximately 719 eV was observed. However, this satellite intensity diminished as more tin was incorporated into the electrode. A loss of Fe^{3+} satellite resolution can result from superposition of the Fe^{2+} satellite at approximately 715 eV and is indicative of Fe_3O_4 character.[28] Introduction of tetravalent Sn ions into the hematite lattice by either substitution or by occupation of vacant interstitial sites requires partial reduction of Fe to maintain charge neutrality, and could account for the observed satellite behavior.[29, 30] It has been proposed that the mutual existence of Fe in two valence states creates a hopping mechanism for conductivity that may contribute to improved PEC performance.[30]

Another interesting feature revealed by XPS was the presence of substantial quantities (2-5 at. %) of sodium on the surface of films after annealing (Fig. S3). It is well known from work on copper indium diselendide (CIS) photovoltaics that Na rapidly diffuses out of soda lime glass at these temperatures, playing beneficial roles with respect to CIS growth and electronic properties.[31] However, no sodium was detected when photoanodes were re-examined after photoelectrochemical evaluation. It is concluded that Na dissolved into the electrolyte during testing, suggesting that Na was loosely bound on the hematite surface and does not impact the photoelectrochemical performance. In contrast, tin levels observed after PEC evaluation were nominally unchanged, showing that it is chemically bound within the hematite lattice as discussed above.

Reducing the activation threshold to 600 °C is an important advance because it permits use of low cost glass. A detrimental consequence of elevated annealing with standard glass is loss of transmission as shown in Figure 4. Films heated above 600 °C suffered a substantial reduction in transmission at wavelengths > 600 nm. This would limit the use of tandem architectures to provide the extra potential required by hematite for the hydrogen evolution reaction.[32] At 600 °C/5 minutes, the long wavelength transmission is nearly identical to that of an uncoated FTO substrate. While the transparency is

somewhat attenuated with increased time, >80% average transmission in this region is retained even after 8 hours. Similar to previous reports,[19] annealing also increased the absorption of the hematite layer. The absorption coefficient was 2 – 4 times greater in samples with higher Sn content, and the difference increases approaching the band gap. For samples annealed at 600 °C the optical penetration depth at 500 nm decreased from 200 to 60 nm as the annealing time was increased from 5 minutes to 8 hours. This is responsible in part for the improved PEC performance, since holes are being generated closer to the electrolyte surface. Despite the enhanced absorption, a Tauc analysis showed that the optical band gap did not change with Sn doping. Assuming either a direct or indirect transition resulted in similar values that were close to the expected 2.1 eV (Fig. S4).

There are a number of mechanisms that may contribute to the dramatic performance improvements with annealing observed in this and related work.[19, 20] As just discussed, the increased absorption coefficients are beneficial, but cannot account for the two order of magnitude increase in photocurrent. There were no significant changes in the XRD patterns to suggest that alterations in crystal structure are responsible (Fig. S1). The phenomenological characteristic that is best correlated with observed improvements with both temperature and time is tin diffusion. A simple explanation is that Sn dopes the hematite films in an analogous manner to its fellow group IV element silicon.[23, 33] As discussed above, the high resolution XPS spectra provide evidence that Sn is occupying Fe sites, and introducing some +2 character. Most leading hematite electrodes are highly doped compounds, and numerous elements (Si, Ti, Pt, Cr, Mo, Al) have been shown to be beneficial.[11, 17, 18, 23-25, 33] High levels of doping reduce the Debye length in hematite to below 1 nm, which has been suggested to improve charge transport and separation.[24]

To further investigate the role of doping a Mott-Schottky analysis was performed at 500 Hz (Fig. S5). There were two major points learned from the analysis. First, all of the films displayed a flat band

potential of ~0.4 V vs RHE regardless of the annealing condition, which is consistent with literature reports for hematite thin films.[24, 25] Somewhat surprising is that the slope in the linear region was largely unaffected by the choice of annealing conditions, varying by no more than a factor of 3. However this is consistent with studies of ceramic samples, which showed little change in conductivity with Sn doping when increased beyond 1 at. %.[30] The best performing photoanode (750 °C/5 minute) had the steepest slope, implying it has the lowest donor density. However, quantitative assessment of donor density is complicated by the mesoporous nature of these photoanodes since the electrochemically active area differs significantly from the geometric area (Fig. 2). In fact, variations in morphology may fully account for the small differences observed. Assuming a planar configuration, the donor density in these samples is estimated to be on the order of ~5 x 10^{20} /cm^3, again consistent with literature reports of Sn-doped films.[30] While doping may be a contributor, there does not appear to be a significant correlation between the donor density and either the Sn concentration or the PEC performance.

It seems unlikely that the 100-fold improvement in PEC performance with annealing can be attributed solely to increased light absorption and enhanced film conductivity. An important contributor to activation may be related to electron transport at the hematite/FTO interface. An unmodified hematite/FTO interface appears to be a major barrier to performance, with traps or defect states at this junction serving as efficient recombination centers that prevent electron extraction to the cathode. To achieve best performance with their APCVD material, Grätzel's group deposits an ultrathin silica layer on the FTO prior to hematite deposition.[8] Similarly, the use of a tetra-ethyl orthosilicate monolayer allowed ultrathin hematite films to be deposited conformally as opposed to by island growth, which significantly enhanced performance.[22] It has also been shown that a 5 nm interfacial layer of SnO_2 greatly improved the photoresponse of hematite films deposited on FTO by ultrasonic spray pyrolysis.[11] In fact, the presence of this interfacial layer was found to be a more important factor than silicon doping.

An important consequence of Sn diffusion that accompanies thermal annealing may be the creation of an improved hematite/FTO interface that promotes efficient electron transport. Removal of this barrier may be a significant contributor to the activation reported in this and related work.

The abrupt jump in photocurrent following annealing is very similar to the results reported by Sivula et al.,[19] although in that case 800 °C was required for activation. In more recent work a titanium dopant was introduced to the colloid suspension, but the temperature requirement for activation remained unchanged.[20] One reason for the difference in activation temperature between these two systems may be related to film thickness. The photoanodes described here were ~200 nm thick, as opposed to the 500-1000 nm films produced using colloids. However, we examined the sensitivity of our process to film thickness over the range of 100 – 400 nm by varying the CBD process, and found very little difference in PEC response. A second reason is that the colloidal approach begins with crystalline hematite nanoparticles, and it may be more difficult to introduce and/or activate dopants using this material as opposed to the nanorods produced by CBD, which are not fully oxidized prior to the annealing step. A third possibility is related to differences in pre-anneal morphology between these two nanostructures. It is expected that electron transport in the mesoporous network produced by colloidal synthesis would require electron hopping from particle to particle, not unlike the process that occurs in dye-sensitized solar cells.[34] The high temperature requirements may reflect the threshold needed to sinter these particles with sufficient connectivity for electron transport. In contrast, a natural byproduct of the nanorod geometry produced by CBD is an inherent pathway for electron transport. Further experimental comparisons would be required to isolate which, if any, of these proposed factors actually contribute to the 200 °C reduced activation threshold.

To summarize, it is shown that proper annealing activates the PEC performance of hematite nanorod arrays. Photoanodes display low onset potentials and the photocurrent density was enhanced by more than 100-fold over previous reports. This activation could be achieved in minutes at high temperature, or after several hours at 600 °C. Reducing the temperature threshold to 600 °C is of practical significance, enabling the use of standard glass. Improved PEC behavior was correlated with substantial changes in both surface morphology and Sn incorporation from the underlying FTO layer. Increased absorption allows electron hole pairs to be generated closer to the electrolyte interface, but the marked enhancement is attributed to improved electron transport through both the hematite itself and at its interface with the FTO contact. While these results present a significant breakthrough in demonstrating the promise of this architecture, considerable opportunities remain for improvement. Further advancements through morphology control, interface engineering, and the integration of electro-catalysts are being pursued to meet this challenge.

Experimental Section:

Nanorod thin films were deposited onto fluorine-doped tin oxide (FTO) coated glass substrates (Hartford Glass Co, TEC-15) using chemical bath deposition. Substrates were placed in an aqueous salt solution containing 0.15 M $FeCl_3$ and 1.0 M $Na(NO)_3$ maintained at 90 °C for between 1 - 5 hours. Nanorod layers ranging from 100 - 400 nm (by profilometry) were examined, though within this range, film thickness did not appreciably impact PEC behavior. The samples were annealed in air in a box furnace as a function of time and temperature. The furnace was ramped at 25 °C/min to the desired setpoint and maintained for the intended time, and then turned off and allowed to cool naturally, which dropped the temperature below 400 °C in a matter of minutes.

FESEM characterization of the films was performed on a JEOL JSM-7000F microscope operating at 5 keV. The crystalline structure was evaluated with a Seimens Kristalloflex 810 XRD using Cu Kα radiation. A Kratos XPS with a monochromatic Al Kα source was used to study the surface composition of the films. Both survey (160 eV pass energy) and high-resolution scans (40 eV pass energy) were performed. XPS spectra were aligned on the basis of adventitious carbon 1s at 286.4 eV and fit with a Shirley background and Voigt line shapes. Surface compositions were estimated with standard relative sensitivity factors and reported on a metals basis (Sn/Sn+Fe) to minimize complications from adventitious C and O. Transmittance in the UV-visible range was collected with a Stellernet SD200 fiber optic spectrophotometer using a FTO substrate as reference.

The measurements of photocurrent were carried out using a custom photoelectrochemical (PEC) cell, a Gamry G300 potentiostat, and a Newport solar simulator. The PEC cell consisted of the working electrode (FTO/hematite), a platinum mesh counter electrode, and a saturated calomel reference electrode. An aqueous solution of 1 M NaOH served as the electrolyte. AM 1.5 simulated sunlight from an appropriately filtered 450 W xenon lamp was supplied through a flat fused glass window onto the front side of the photoanode surface at a measured intensity of 87 mW/cm^2 . The area of illumination of 0.95 cm^2 was defined by the Teflon fixture used to mount the working electrode. The photocurrent was measured while sweeping the applied potential at 50 $mV\ s^{-1}$ between -1 and +1 V. All potentials are corrected for pH and reported against the reversible hydrogen electrode (RHE). Impedance data was collected at frequencies ranging from 10 - 5000 Hz. The similar response of photoanodes processed at different annealing conditions shown in Fig. S5 was consistent throughout the frequency range.

Supporting Information. Supporting Information is available from the Wiley Online library or from the author.

Acknowledgement. This research was supported by the Shared Research Program of the Center for Revolutionary Solar Photoconversion as well as Science Foundation Ireland's Strategic Research Cluster in Solar Energy Conversion (07/SRC/B1160). CAW acknowledges Science Foundation Ireland for support through an E.T.S. Walton visitor fellowship. Material characterization employed the shared facilities of the Renewable Energy Materials Research and Engineering Center (DMR-0820518) at CSM and the Nano Imaging and Material Analysis Centre at UCD.

References

1. Z. B. Chen, T. F. Jaramillo, T. G. Deutsch, A. Kleiman-Shwarsctein, A. J. Forman, N. Gaillard, R. Garland, K. Takanabe, C. Heske, M. Sunkara, E. W. McFarland, K. Domen, E. L. Miller, J. A. Turner, H. N. Dinh, *J. Mater. Res.* **2010**, *25*, 3.
2. S. Tilley, M. Cornuz, K. Sivula, M. Grätzel, *Angew. Chem. Int. Ed.* **2010**, *122*, 6549.
3. D. K. Zhong, J. Sun, H. Inumaru, D. R. Gamelin, *J. Am. Chem. Soc.* **2009**, *131*, 6086.
4. A. Kleiman-Shwarsctein, Y. S. Hu, G. D. Stucky, E. W. McFarland, *Electrochem. Commun.* **2009**, *11*, 1150.
5. K. Itoh, J. O. M. Bockris, *J. Electrochem. Soc.* **1984**, *131*, 1266.
6. J. H. Kennedy, J. K. W. Frese, *J. Electrochem. Soc.* **1978**, *125*, 723.
7. N. J. Cherepy, D. B. Liston, J. A. Lovejoy, H. Deng, J. Z. Zhang, *J. Phys. Chem. B* **1998**, *102*, 770.
8. A. Kay, I. Cesar, M. Gratzel, *J. Am. Chem. Soc.* **2006**, *128*, 15714.
9. S. K. Mohapatra, S. E. John, S. Banerjee, M. Misra, *Chem. Mater.* **2009**, *21*, 3048.
10. P. Yang, R. Yan, M. Fardy, *Nano Lett.* **2010**, *10*, 1529.
11. R. van de Krol, Y. Q. Liang, J. Schoonman, *J. Mater. Chem.* **2008**, *18*, 2311.
12. L. Vayssieres, N. Beermann, S. E. Lindquist, A. Hagfeldt, *Chem. Mater.* **2001**, *13*, 233.
13. Y. Y. Fu, R. M. Wang, J. Xu, J. Chen, Y. Yan, A. V. Narlikar, H. Zhang, *Chem. Phys. Lett.* **2003**, *379*, 373.
14. X. Wen, S. Wang, Y. Ding, Z. L. Wang, S. Yang, *J. Phys. Chem. B* **2004**, *109*, 215.
15. N. Beermann, L. Vayssieres, S.-E. Lindquist, A. Hagfeldt, *J. Electrochem. Soc.* **2000**, *147*, 2456.
16. T. Lindgren, H. Wang, N. Beermann, L. Vayssieres, A. Hagfeldt, S.-E. Lindquist, *Sol. Energy Mater. Sol. Cells* **2002**, *71*, 231.
17. Y. S. Hu, A. Kleiman-Shwarsctein, A. J. Forman, D. Hazen, J. N. Park, E. W. McFarland, *Chem. Mater.* **2008**, *20*, 3803.
18. A. Kleiman-Shwarsctein, Y.-S. Hu, A. J. Forman, G. D. Stucky, E. W. McFarland, *J. Phys. Chem. C* **2008**, *112*, 15900.
19. K. Sivula, R. Zboril, F. Le Formal, R. Robert, A. Weidenkaff, J. Tucek, J. Frydrych, M. Gratzel, *J. Am. Chem. Soc.* **2010**, *132*, 7436.
20. J. Brillet, M. Grätzel, K. Sivula, *Nano Lett.* **2010**, *10*, 4155.
21. M. G. Walter, E. L. Warren, J. R. McKone, S. W. Boettcher, Q. Mi, E. A. Santori, N. S. Lewis, *Chem. Rev.* **2010**, *110*, 6446.
22. F. Le Formal, M. Gratzel, K. Sivula, *Adv. Funct. Mater.* **2010**, *20*, 1099.
23. I. Cesar, A. Kay, J. A. Gonzalez Martinez, M. Gratzel, *J. Am. Chem. Soc.* **2006**, *128*, 4582.
24. M. L. Zhang, W. J. Luo, Z. S. Li, T. Yu, Z. G. Zou, *Appl. Phys. Lett.* **2010**, *97*, 042105.
25. A. Kleiman-Shwarsctein, M. N. Huda, A. Walsh, Y. F. Yan, G. D. Stucky, Y. S. Hu, M. M. Al-Jassim, E. W. McFarland, *Chem. Mater.* **2010**, *22*, 510.
26. R. Hansson, P. C. Hayes, E. Jak, *Can. Metall. Quart.* **2004**, *43*, 545.
27. M. Sorescu, L. Diamandescu, D. Tarabasanu-Mihaila, V. S. Teodorescu, B. H. Howard, *J. Phys. Chem. Solids* **2004**, *65*, 1021.
28. T. Fujii, F. M. F. de Groot, G. A. Sawatzky, F. C. Voogt, T. Hibma, K. Okada, *Phys. Rev. B* **1999**, *59*, 3195.
29. F. J. Berry, C. Greaves, J. G. McManus, M. Mortimer, G. Oates, *J. Solid State Chem.* **1997**, *130*, 272.
30. V. M. Aroutiounian, V. M. Arakelyan, G. E. Shahnazaryan, H. R. Hovhannisyan, H. Wang, J. A. Turner, *Solar Energy* **2007**, *81*, 1369.
31. S. Niki, M. Contreras, I. Repins, M. Powalla, K. Kushiya, S. Ishizuka, K. Matsubara, *Prog. Photovolt: Res. Appl.* **2010**, *18*, 453.
32. J. Brillet, M. Cornuz, F. Le Formal, J. H. Yum, M. Gratzel, K. Sivula, *J. Mater. Res.* **2010**, *25*, 17.
33. I. Cesar, K. Sivula, A. Kay, R. Zboril, M. Graetzel, *J. Phys. Chem. C* **2008**, *113*, 772.
34. A. Hagfeldt, G. Boschloo, L. Sun, L. Kloo, H. Pettersson, *Chem. Rev.* **2010**, *110*, 6595.

Figure 1. Photocurrent density as a function of applied potential for selected annealing conditions. *Inset* – Oxygen evolution current density (J_{OER}) as a function of annealing time and temperature.

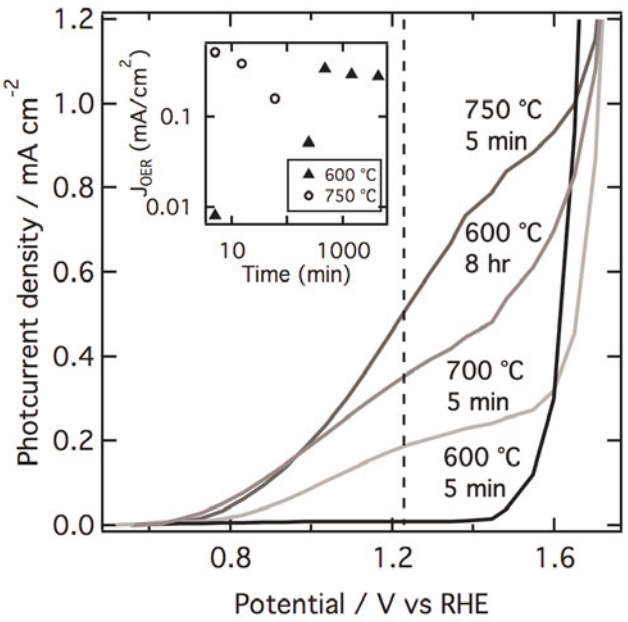

Figure 2. Morphology of hematite nanostructure annealed for the conditions described in Fig. 1. The scale bar applies to all four images.

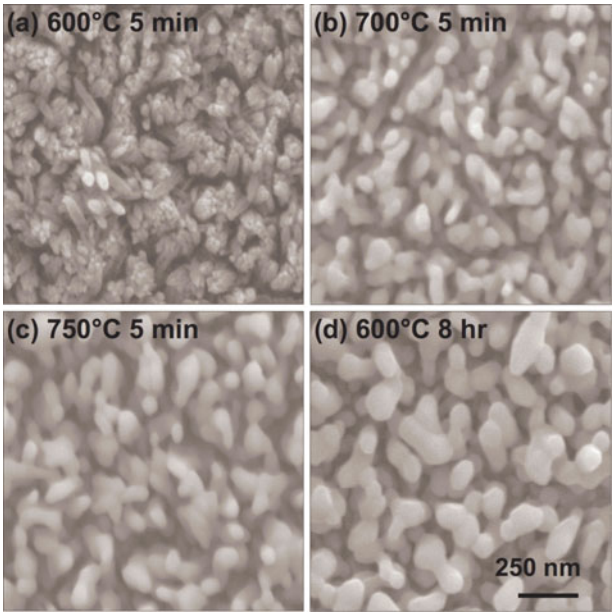

Figure 3. High resolution XPS spectra showing (a) the Sn 3d region and (b) the Fe 2p region obtained from annealed hematite photoanodes.

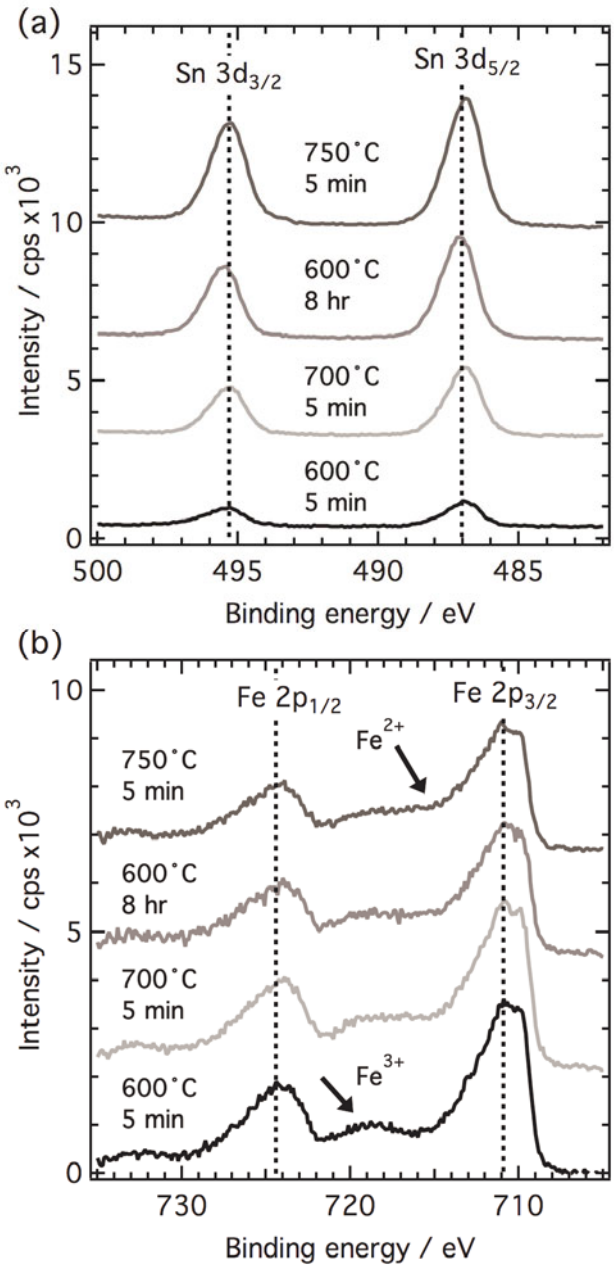

Figure 4. Transmission spectra obtained from annealed hematite photoanodes.

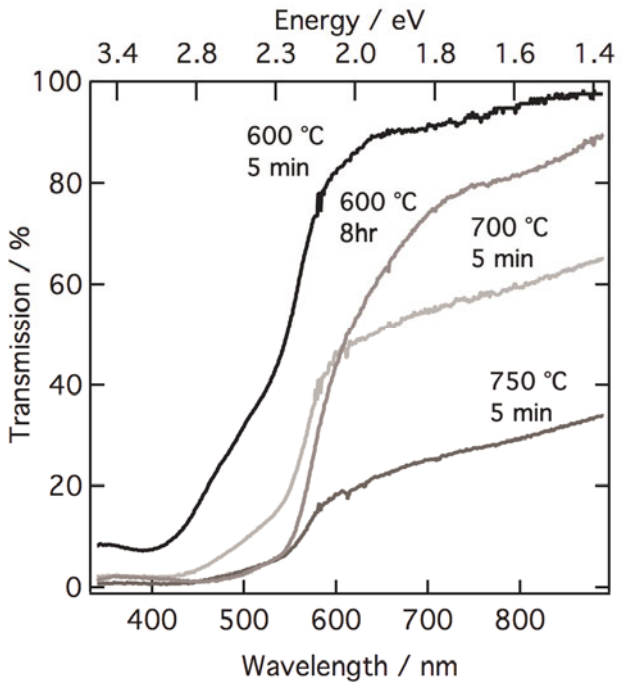

Supporting Information:

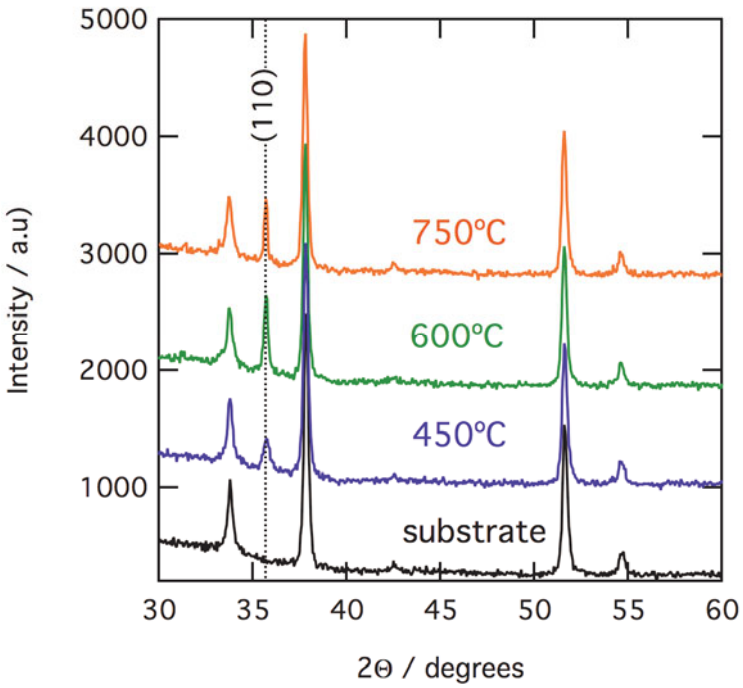

Figure S1: XRD spectra of samples heated at 450 °C/1 hr, 600 °C/5 min, and 750 °C/5 min in comparison to a bare FTO substrate.

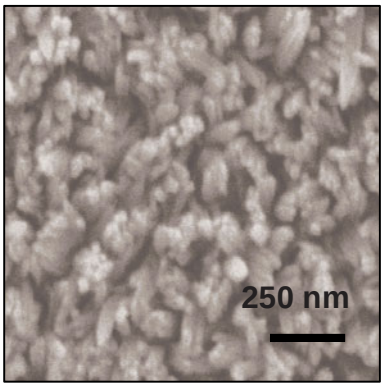

Figure S2: FESEM image of sample produced by CBD and not annealed.

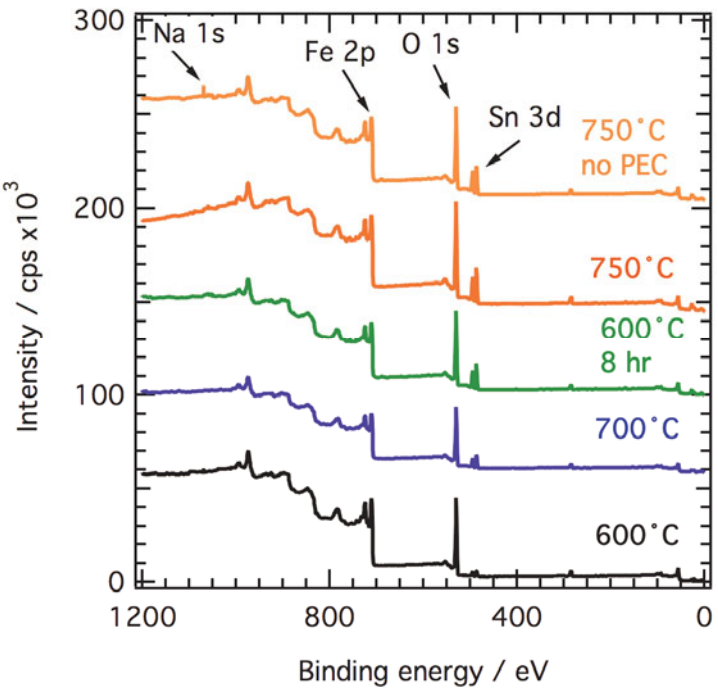

Figure S3: Survey XPS spectra of hematite samples annealed for 5 minutes at 600, 700, and 750 °C in comparison to a sampled annealed at 600 °C for 8 hours. Also given is a spectra obtained on a sample that had not been exposed to PEC characterization displaying sodium.

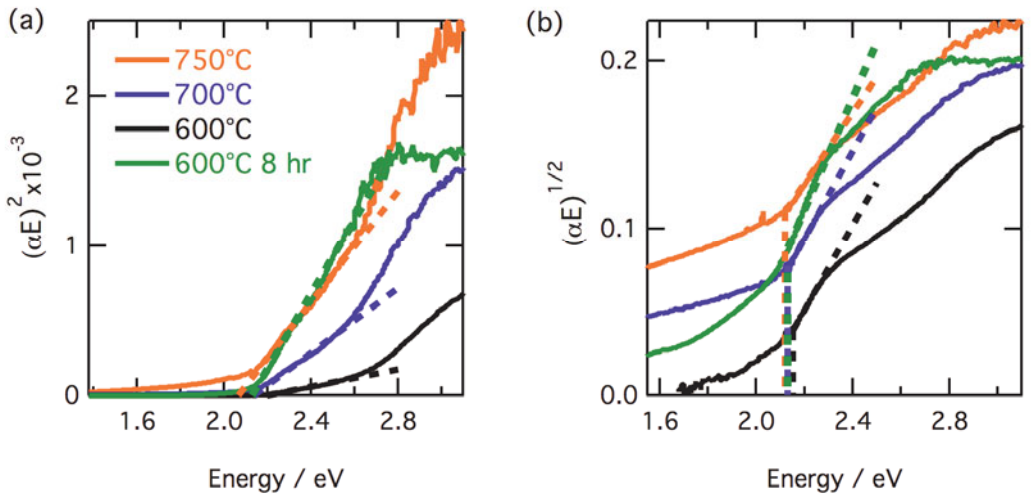

Figure S4: Tauc analysis assuming a (a) direct transitions and (b) indirect transitions of hematite samples annealed for 5 minutes at 600, 700, and 750 °C in comparison to a samples annealed at 600 °C for 8 hours.

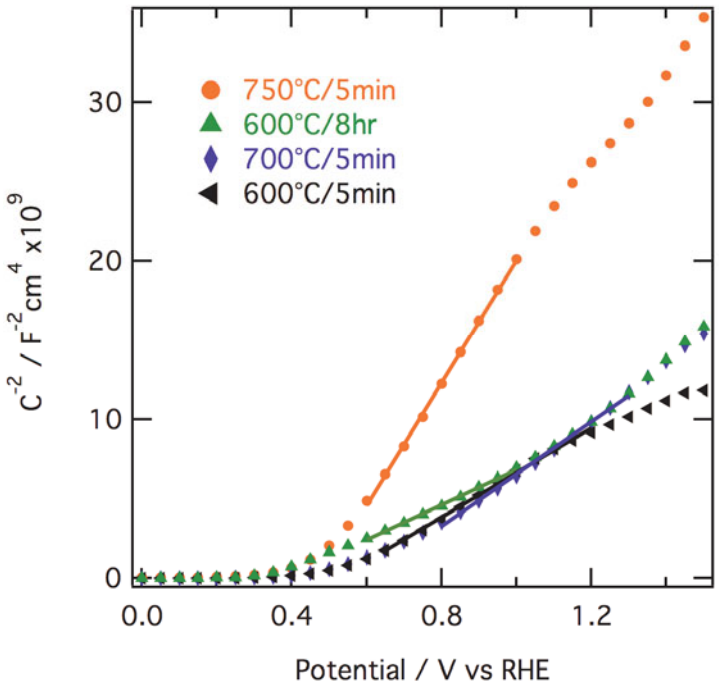

Figure S5. Mott-Schottky analysis of annealed hematite photoanodes. All electrodes exhibited a flat band potential of approximately 0.4 V vs RHE.